Annals of Nuclear Energy 73 (2014) 455–464

Contents lists available at ScienceDirect

Annals of Nuclear Energy

journal homepage: www.elsevier.com/locate/anucene

Quasi-differential neutron scattering from ^{238}U from 0.5 to 20 MeV

A.M. Daskalakis [a,*], R.M. Bahran [a], E.J. Blain [a], B.J. McDermott [a], S. Piela [a], Y. Danon [a], D.P. Barry [b], G. Leinweber [b], R.C. Block [b], M.J. Rapp [b], R. Capote [c], A. Trkov [d]

[a] Gaerttner LINAC Center, Rensselaer Polytechnic Institute, Troy, NY 12180, United States
[b] Bechtel Marine Propulsion Corporation, Knolls Atomic Power Laboratory, P.O. Box 1072, Schenectady, NY 12301, United States
[c] International Atomic Energy Agency, NAPC-Nuclear Data Section, Austria
[d] Jozef Stefan Institute, Slovenia

ARTICLE INFO

Article history:
Received 2 June 2014
Received in revised form 14 July 2014
Accepted 15 July 2014
Available online 8 August 2014

Keywords:
RPI
Uranium-238
Measurement
Neutron scattering
Time-of-flight experiment
Benchmark

ABSTRACT

The Rensselaer Polytechnic Institute Linear Accelerator was used to produce a pulsed neutron beam that was incident on a ^{238}U scattering sample 30 m from the source. Eight liquid scintillator (EJ-301) proton recoil fast neutron detectors located at several angles surrounding the sample were positioned at a distance 0.5 m. Neutrons resulting from elastic scattering, inelastic scattering, and fission reactions were recorded as a function of time-of-flight. Pulse shape analysis including a new gamma misclassification correction was used to reduce erroneous counts from gamma events produced from fission and inelastic scattering reactions. The experimental data were simulated using an improved model of the Rensselaer Polytechnic Institute neutron scattering system that included individual detector efficiencies and neutron flux shape. The experimental data were compared with several evaluated nuclear data libraries using a figure-of-merit. Overall, the JENDL-4.0 evaluation provided the best agreement with the ^{238}U experimental data. Furthermore, the Rensselaer Polytechnic Institute scattering model was used to constrain uncertainties that allowed for improvements to a new ^{238}U evaluation.

1. Introduction

^{238}U is a significant component of the nuclear fuel cycle that includes nuclear fuel enrichment facilities, nuclear powered light water reactors, and spent fuel storage. To safely design these systems, accurate ^{238}U nuclear properties are required. Nuclear properties of ^{238}U, including neutron interaction probabilities and angular distributions of secondary particles, are found in evaluated data libraries such as ENDF/B-VII.1 (Chadwick et al., 2011) and its predecessor ENDF/B-VI.8 (NNDC, 2013), JEFF-3.1 (Koning et al., 2006), and JENDL-4.0 (Shibata et al., 2011). Libraries vary based on the experimental data or nuclear models used in the construction of their evaluation. For example, the Maslov evaluation (Maslov et al., 2003) compared the angular distribution of elastically scattered neutrons from ^{238}U experimental measurements with nuclear models and was incorporated into ENDF/B-VII.1. Similarly, the CCONE (Shibata et al., 2011) code was used to determine the neutron elastic angular distribution of ^{238}U for JENDL-4.0. Both of the aforementioned evaluations relied on nuclear models to accurately represent neutron interactions with ^{238}U nuclei. Experimental nuclear data provide a means to measure interaction probabilities and validate nuclear models.

Nuclear data can be obtained from many different experimental techniques designed to isolate and measure specific reactions. Smith et al. produced near mono-energetic neutron beams to perform double differential scattering experiments with a thin sample at discrete angles to determine the energy dependent angular distribution (Smith et al., 1978). Integral critical benchmark systems use the combined effects of all neutron induced events to quantify agreement with known standards (Mosteller and MacFarlane, 2006). The pros and cons of double differential scattering measurements and integral experiments were discussed in Saglime et al. (2010) and Saglime (2009).

The Rensselaer Polytechnic Institute (RPI) neutron scattering system consisted of 8 detectors that were positioned around a scattering sample measuring the response from a range of neutron energies at several angles. The term "quasi-differential" signifies that the measurements were of neutrons that may have been scattered numerous times in the sample, the detectors were located at a relatively close distance from the scattering sample and subtended a finite range of solid angle, and the neutron source consisted of a spectrum of incident energies. The multiple scattering provided increased signal strength that reduced experimental

* Corresponding author.
E-mail address: daskaa@rpi.edu (A.M. Daskalakis).

http://dx.doi.org/10.1016/j.anucene.2014.07.023
0306-4549/

uncertainty (Barry et al., 2013). The relatively short scattering flight path and relatively large detectors improved the neutron count rate. These features enable the benchmarking of differential scattering cross-section data in the energy range from 0.5 to 20 MeV and were used to benchmark several nuclear data libraries (Saglime et al., 2010). Variations between the experimental data and MCNP calculations may indicate areas where improvement in the nuclear data libraries could be made.

Previously, the RPI scattering system was compared to FIGARO at Los Alamos National Lab (Saglime et al., 2010) and was used to compare beryllium (Saglime, 2009), molybdenum (Saglime, 2009), and zirconium (Barry et al., 2013) experimental measurements with evaluated nuclear data libraries. A detailed description of the experimental technique has been previously published (Saglime et al., 2010; Saglime, 2009; Barry et al., 2013).

Four major improvements have been made to the RPI neutron scattering system since our previous publication (Barry et al., 2013). The first of these improvements was to perform new in-beam measurements that determined the energy-dependent intrinsic efficiency for each neutron detector. Secondly, the neutron flux shape was characterized using the combination of ^{235}U fission chamber and in-beam detector responses. The third improvement was the development of a single normalization factor for all MCNP simulations. Lastly, pulse shape analysis (PSA) was improved to minimize the number of gammas erroneously treated as neutrons. Improved PSA was crucial to overcome the additional background posed by measurements of samples that have high gamma background from fission and inelastic scattering. This improved method was used to compare experimental data to evaluated nuclear data libraries.

Each detector's calculated efficiency was incorporated and verified through MCNP simulations (MCNP, 2005). Similar to previous experiments a graphite reference sample was measured and modeled with MCNP.

2. Experimental setup

The RPI Linear Accelerator (LINAC) produced electrons with energies up to 60 MeV and collided them with a neutron producing tantalum target (Overberg et al., 1999). Operated at 400 pulses per second the average current on target was 8 μA with an electron burst width of 5 ns. The electrons produced bremsstrahlung radiation within the target that interacted with the tantalum plates, creating a pulse of neutrons through the (γ, n) reaction. A continuous energy neutron distribution similar to an evaporation spectrum was produced (Barry et al., 2013). The neutrons escaped the target and traveled along an evacuated flight path to a distance of 30.07 m where the scattering sample, either the graphite reference or ^{238}U, was positioned in the RPI scattering system. An illustration of the experimental setup is shown in Fig. 1. A 1.9 cm thick depleted uranium filter was placed in the beam to reduce the intense gamma flash radiation produced by the target. Collimators were positioned along the evacuated flight path to create a neutron beam diameter of under 7.62 cm incident on the scattering sample. Two moderated fission chambers (shown in Fig. 1) were used to monitor fluctuations of the neutron beam intensity throughout the experiment. Both fission chambers were located ≈9 m from the neutron producing target.

For the scattering experiment, an array of eight ELJEN Technologies EJ-301 liquid scintillator proton recoil fast neutron detectors were arranged at various scattering angles relative to the incident neutron beam. Each detector's position was chosen to maximize distance between detectors. The scattering angles were chosen based on discrepancies between libraries. A detailed view of the eight EJ-301 detectors surrounding a scattering sample is shown in Fig. 2. Throughout each experiment two detectors were placed at each angle. The EJ-301 liquid scintillators have properties that allow pulse shape discrimination used for neutron spectroscopy

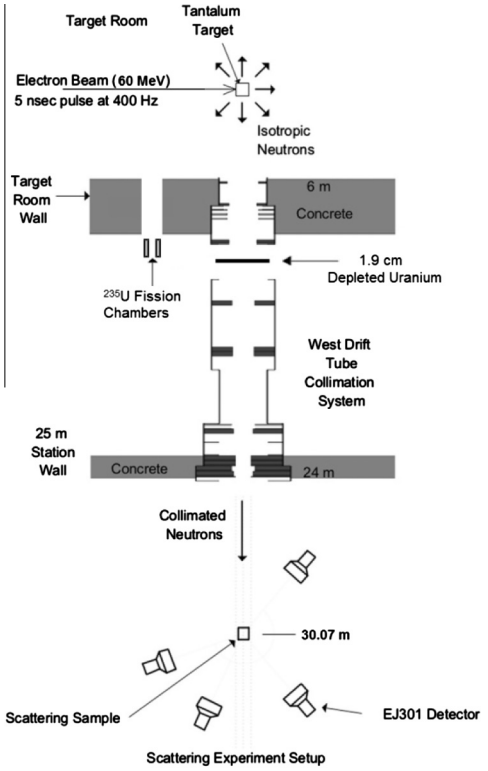

Fig. 1. Overview of quasi-differential scattering experimental setup. Detectors located at 0.50 m from a scattering sample record neutron events in TOF originating from the tantalum target 30.07 m away. Note: The drawing is not to scale. Only four EJ-301 detectors are shown. Vacuum pipes and Mylar vacuum windows are omitted. An additional vacuum pipe measuring 365 cm was positioned between the scattering sample and the concrete wall for the second ^{238}U scattering experiment.

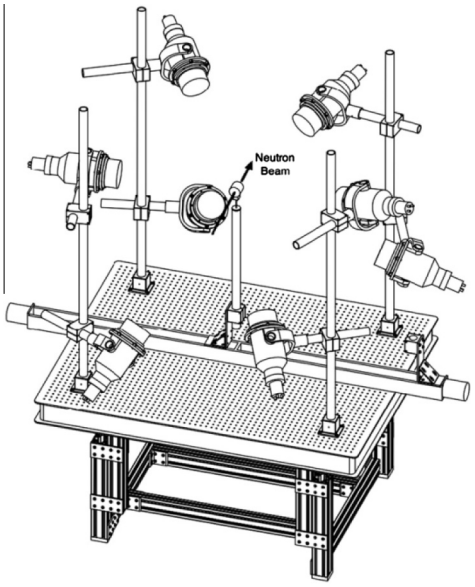

Fig. 2. Detailed view of eight EJ-301 detectors surrounding a scattering sample. The detectors were secured using aluminum rods that were positioned on a 152 × 152 cm (5 ft × 5 ft) optical table. Each detector's position was chosen to maximize distance between itself and other detectors (Barry et al., 2013).

(chap. 8 of Knoll (2000)). The dimensions of each detector are 12.7 cm in diameter by 7.62 cm in length. Each detector is coupled to a 12.7 cm diameter Photonis XP4572/B photomultiplier tube (PMT). Negative high voltage was supplied to each detector by a CAEN unit, model 1733 N. The gain of each scattering detector was aligned at the Compton edge of 0.511 MeV annihilation gammas from a ^{22}Na source by adjusting the PMT high voltage. Throughout the experiment the gain alignment was periodically checked to ensure that the detector gains were not drifting.

In order to record the neutron time-of-flight (TOF) the raw analog signals from the detectors were fed into an Agilent-Acqiris AP240 digitizer. Each detector signal was digitized by an 8-bit digitizer and transferred by an onboard field-programmable gate array (FPGA) only if the pulse exceeded a predefined threshold (Saglime, 2009). The transferred digital signal consisted of 120 data points sampled at 1 GHz. The 120 ns collection interval was determined by the EJ-301 liquid scintillator response time. The data acquisition system was capable of providing a maximum of 128,000 transfers per second (Saglime, 2009); however, during the experiment, an average of 2300 transfers per second occurred.

3. Determination of neutron flux shape and detector efficiencies

To improve the accuracy of the MCNP model of the RPI neutron scattering system, a new method was developed to determine the efficiency of each EJ-301 detector. Previously, one efficiency curve for all RPI scattering neutron detectors was determined from SCINFUL modeling of proton-recoil liquid scintillators (SCINFUL, 1998). However, the assumption that all detectors shared identical efficiencies did not account for the observed slight variations in efficiency between the detectors. The energy-dependent flux shape refers to the neutron energy distribution at the target location. The time-dependent neutron flux shape below neutron energy of 1 MeV was measured with a ^{235}U fission chamber positioned in the center of the neutron beam at the scattering sample position 30.07 m from the neutron target. The counting rate of the fission chamber, $R_{fc}(E)$, measured in TOF was used to develop an energy-dependent neutron flux shape, $\phi_{fc}(E)$, for MCNP up to 1 MeV.

$$\phi_{fc}(E) = \frac{R_{fc}(E)}{\sigma_f^{235}(E) \cdot T(E) \cdot k_{fc}} \quad (1)$$

Along with the fission chamber counting rate, the transmission through material in the neutron flight path and fission cross section, $T(E)$ and $\sigma_f^{235}(E)$, respectively, determined the neutron flux shape. The constant, k_{fc}, that consists of ^{235}U number density, ^{235}U thickness, fission chamber efficiency, active surface area of the fission chamber, and total number of LINAC pulses may be included; although, the analysis with MCNP required only the flux shape. Above 1 MeV the ^{235}U measured flux shape agreed with a SCINFUL efficiency developed in Saglime (2009); however, the flux obtained from the EJ-301 had lower counting statistic uncertainties and was used above 1 MeV.

Each detector's measurement was obtained separately, requiring the use of monitors to track fluctuations in neutron beam intensity. Dead-time correction was applied for all in-beam experimental data collected by the EJ-301 detectors and the ^{235}U fission chamber. For any given set of data, the correction never exceeded 5%. The neutron energy-dependent flux shape measured by all EJ-301 detectors, $\phi_{EJ}(E)$, was determined from the averaged count rate, $R_{EJ}(E)$, and calculated SCINFUL efficiency, $\eta_{EJ}(E)$, as presented in the following equation:

$$\phi_{EJ}(E) = \frac{R_{EJ}(E)}{\eta_{EJ}(E) \cdot T(E) \cdot k_{EJ}} \quad (2)$$

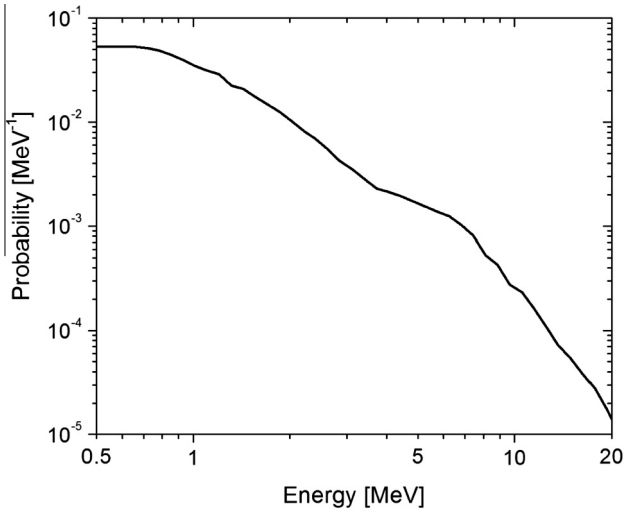

Fig. 3. The source neutron flux, $\phi(E)$, used by MCNP simulations for initial neutron energy. The energy-dependent flux shape was determined using a combination of data using a ^{235}U fission chamber and EJ-301 neutron detectors.

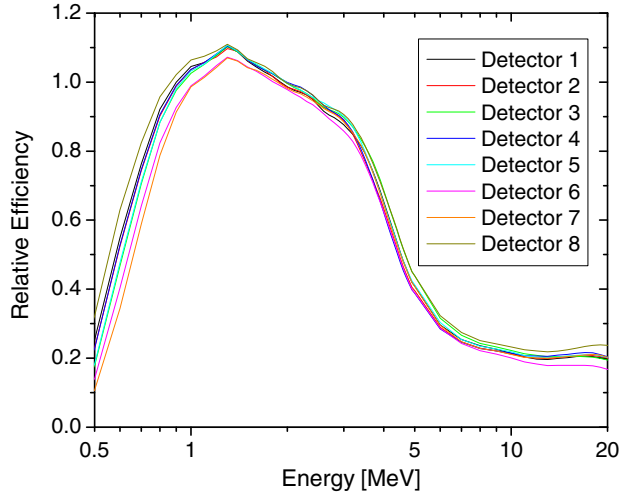

Fig. 4. The relative efficiency, $\eta_i(E)$, for each detector, i, used in the scattering system. There are significant differences between detectors below 1 MeV that must be accounted for to reduce the uncertainty in the normalization factor.

The constant, k_{EJ}, represents the detector surface area and total number of LINAC pulses. A continuous energy-dependent neutron flux shape, $\phi(E)$, was derived from the combination of ^{235}U fission chamber flux shape, $\phi_{fc}(E)$, and EJ-301 flux shape, $\phi_{EJ}(E)$, and was incorporated as the neutron source particle distribution for MCNP. The calculated neutron flux shape, $\phi(E)$, is shown in Fig. 3.

The energy-dependent intrinsic efficiency of each EJ-301 detector was calculated based on its response to the previously determined neutron flux shape. Manipulating Eq. (2) to solve for the detector efficiency yields eight unique energy-dependent results, $\eta_i(E)$, one for each in-beam EJ-301 measurement. To eliminate statistical fluctuations from measured counts each detectors calculated efficiency was smoothed using a Savitzky–Golay smoothing function (Savitzky and Golay, 1964). Fig. 4 shows each detector's relative efficiencies after adjustment for beam fluctuations using monitors. In-beam experiments were modeled in MCNP with all significant structural materials, the detector's intrinsic energy-dependent efficiency, and energy-dependent flux shape modeled at the target location. An F2 surface tally located at the detector position 30.07 m from the source replicated the

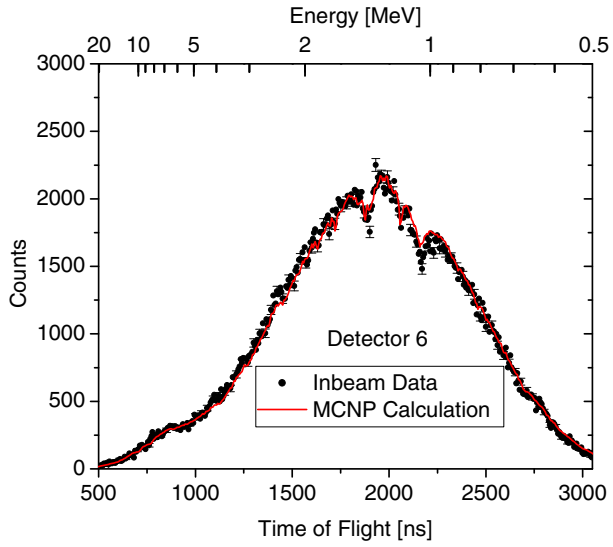

Fig. 5. An in-beam measurement and its MCNP fit based on the calculated efficiency. The energy-dependent flux and energy-dependent efficiency were solved using the response of a ^{235}U fission chamber and the in-beam experimental data shown here. The MCNP simulation replicates the measured response from detector 6.

Table 1
Allocation time for the different samples placed in the neutron beam. The values represented in the table did not vary between the two experimental data sets. The total data acquisition time for each cycle was 31.25 min with ≈100 cycles for each sample.

Sample	Position	Pulses	Time (min)
^{238}U	0	450000	18.75
Graphite	1	150000	6.25
Open	2	150000	6.25

response of each detector. Fig. 5 shows an example of these calculations overlaid on the experimental data. The agreement between MCNP simulations and the in-beam experimental data serves as a verification of the EJ-301 detector's efficiency and measured flux shape.

4. Data collection and analysis

Throughout the experiment several sets of data were collected. A graphite reference sample and ^{238}U were cycled into the center of the neutron beam using a programmable sample changer. Both samples were oriented such that the beam passed through their central axis. The neutron beam diameter was smaller than the diameter of each sample. Background count rate was measured with an open beam where no sample was present in the neutron beam path. Each sample was positioned in the neutron beam for no longer than 20 min, resulting in ≈100 cycles for each sample, including open beam. During each measurement, neutron beam monitors recorded fluctuations in the beam intensity. Allocation time for each sample per cycle for both experimental angle sets is shown in Table 1.

Table 3
Angle of each detector relative to the incident neutron beam. All angles were measured with an accuracy of ±2°.

Detector	Experiment 1	Experiment 2
1	27	45
2	77	60
3	153	153
4	156	156
5	113	130
6	112	130
7	29	45
8	77	60

All data collected by each of the EJ-301 scattering detectors was processed using PSA to discriminate photons from neutrons and to eliminate distorted or saturated pulses. The total neutron counts from the scattering sample at each energy bin were determined by removing the open beam contribution, adjusting for beam fluctuations, and removal of gamma events misclassified as neutron events as shown in the following equation:

$$C_{i,j} = \left(D^S_{i,j} - G^S_{i,j}\right) - \left(D^O_{i,j} - G^O_{i,j}\right) \cdot \frac{M^S}{M^O} \tag{3}$$

The total neutron counts, $C_{i,j}$, recorded by a detector, i, in an energy interval, j, was obtained by subtracting the open beam neutron data, $D^O_{i,j}$, from the sample data, $D^S_{i,j}$. Neutron intensity fluctuations and differences in the measurement times were corrected by the monitor ratios which are defined as monitor counts with the sample in, M^S, to monitors with open beam, M^O. The gamma misclassification correction counts, $G_{i,j}$, were introduced to reduce contributions from gamma events that were falsely categorized as neutrons. The gamma misclassification correction was developed by measuring gamma sources and recording events which the pulse shape analysis classified as neutrons. A curve of the fraction of falsely-classified gamma pulses as a function of the event pulse integral obtained from these measurements was used to determine the gamma misclassification correction. During the time-of-flight measurements the gamma contribution from pulses classified as gammas and this curve were used to obtain the gamma misclassification correction $G_{i,j}$. The gamma misclassification correction counts, $G_{i,j}$, reduced the neutron counts by less than 1% below 5 MeV up to a maximum of about 3% above 5 MeV.

Statistical uncertainty in the number of counts in an energy channel, $\Delta C_{i,j}$, associated with Eq. (3), was found by applying the standard error propagation formula for uncorrelated variables (chap. 3 of Knoll (2000)).

$$\Delta C_{i,j} = \sqrt{D^S_{i,j} + G^S_{i,j} + D^O_{i,j} \cdot \left(\frac{M^S}{M^O}\right)^2 + G^O_{i,j} \cdot \left(\frac{M^S}{M^O}\right)^2 + M^S \cdot \left(\frac{D^O_{i,j} - G^O_{i,j}}{M^O}\right)^2 + \left(D^O_{i,j} - G^O_{i,j}\right)^2 \cdot \left(\frac{M^{S^2}}{M^{O^3}}\right)} \tag{4}$$

To compare the experimental data to MCNP simulations of the experiment, a figure-of-merit (FOM), using the same functional form as the reduced chi-square goodness of fit, was adopted for the entire region-of-interest (ROI), between 0.5 and 20 MeV. A lower value for the FOM indicates better agreement. For all energy bins, the difference between each detector's ^{238}U experimental data and their corresponding MCNP simulations, $MC_{i,j}$, was divided by the experimental uncertainty, $\varepsilon_{i,j}$, represented by;

Table 2
Sample information for the graphite reference and ^{238}U. The mass and number density values in the table reflect that of the entire sample.

Sample	Thickness (cm)	Diameter (cm)	Mass (g)	Number density (atoms/b)
Graphite	7.001 ± 0.002	7.498 ± 0.003	512.87 ± 0.01	0.5925 ± 0.0002
^{238}U	0.979 ± 0.002	7.618 ± 0.002	841.08 ± 0.02	0.0467 ± 0.0002

$$\mathrm{FOM}_i = \frac{1}{n} \cdot \sum_{j=0.5\ \mathrm{MeV}}^{20\ \mathrm{MeV}} \frac{(C_{i,j} - MC_{i,j})^2}{\varepsilon_{i,j}^2} \tag{5}$$

where n represents total number of energy bins in the ROI. Experimental uncertainties, $\varepsilon_{i,j}$, consisted of statistical uncertainty for an energy channel, $\Delta C_{i,j}$, and the fractional normalization factor uncertainty, ε_N. The relationship between these two quantities is represented mathematically by the following equation:

$$\varepsilon_{i,j}^2 = \Delta C_{i,j}^2 + (C_{i,j} \cdot \varepsilon_N)^2 \tag{6}$$

The normalization factor and its associated uncertainty are described in greater detail in the next section. Furthermore, a sensitivity analysis was performed by increasing or decreasing the experimental data $C_{i,j}$ by $\Delta C_{i,j}$ in Eqs. (5) and (6). It was concluded that all FOM within 0.6 of the best fitting evaluation were indistinguishable for given experimental uncertainties.

5. Quasi-differential scattering measurements

All measurements performed with the RPI scattering system involve a TOF experiment using a continuous energy neutron distribution similar to an evaporation spectrum (Barry et al., 2013). The total neutron flight path distance consists of two parts: from the neutron target to the sample, $L_1 = 30.07 \pm 0.02$ m (Saglime et al., 2010) and following a scattering event from the sample to detector, $L_2 = 0.50 \pm 0.01$ m. A neutron of energy E_1 traversed the distance L_1 with time t_1 and exits the collision with energy E_2 and traverses the path L_2 in time t_2. The total TOF, t, is expressed as:

$$t = t_1 + t_2 = \frac{\left(\frac{L_1}{c}\right)}{\sqrt{1 - \left(\frac{m_n c^2}{E_1 + m_n c^2}\right)^2}} + \frac{\left(\frac{L_2}{c}\right)}{\sqrt{1 - \left(\frac{m_n c^2}{E_2 + m_n c^2}\right)^2}} \tag{7}$$

where c is the velocity of light in a vacuum and m_n is the rest mass of the neutron. After the neutron undergoes an elastic interaction with the scattering sample the energy loss incurred was negligible (true for heavy nuclei; for light nuclei this assumption cannot be made), or $E_1 \approx E_2$ and thus, $t_2 << t_1$. The effective flight path is now defined as $L = L_1 + L_2$. Both L and $t = t_1 + t_2$ are used to obtain an effective incident neutron energy at TOF, t.

$$E(t) \approx m_n c^2 \cdot \left(\frac{1}{\sqrt{1 - \left(\frac{L}{c \cdot t}\right)^2}} - 1 \right) \tag{8}$$

This representation was used to calculate the incident neutron energy channel, j, for experimental data and the time-dependent MCNP simulations. The approximations provided an effective incident energy that helps interpret the data.

The reference sample is a high purity cylinder of graphite with a 7.5 cm diameter and 7 cm thickness (Saglime, 2009) placed with its cylindrical axis along the neutron beam axis. Graphite was used as the reference sample due to carbon's good agreement among ENDF/B-VII.1, ENDF/B-VI.8, and JEFF-3.1 (Saglime et al., 2010; Barry et al., 2013). The response of all detectors to neutron interactions with the graphite reference sample was modeled using MCNP. The ENDF/B-VII.1 evaluation of graphite was used in the MCNP calculations. A normalization factor was applied to all MCNP calculations to compare them to the experimental data. To determine the normalization factor, the following method was used. First, for each detector, the monitor normalized counts for the graphite reference sample integrated over all TOF between 0.5 and 20 MeV was divided by the respective MCNP-calculated response. These values for all eight detectors were then averaged resulting in the normalization factor. The normalization uncertainty that was introduced in Eq. (6), ε_N, was the standard deviation of the distribution of these normalization factors. Detailed information regarding the graphite reference can be found in Table 2. Fig. 6 shows the measured graphite data and calculated MCNP response for detector 2 and detector 3, located at 60° and 153°, respectively, for the second set of experimental angles. The FOM for all graphite measurements are available in Table 4. The agreement between MCNP simulations and the experimental data are very good and serve as a verification of the data analysis and modeling methodology.

The depleted uranium sample (0.2% ^{235}U) was cylindrical with a 7.6 cm diameter and 0.98 cm thickness placed with its cylindrical axis along the neutron beam axis. Detailed information regarding the ^{238}U sample can be found in Table 2. The normalization factor was applied to the MCNP calculations for comparison with experimental data. The calculated contribution from 0.2% ^{235}U and other impurities was negligible for the ROI and at each angle. Over the

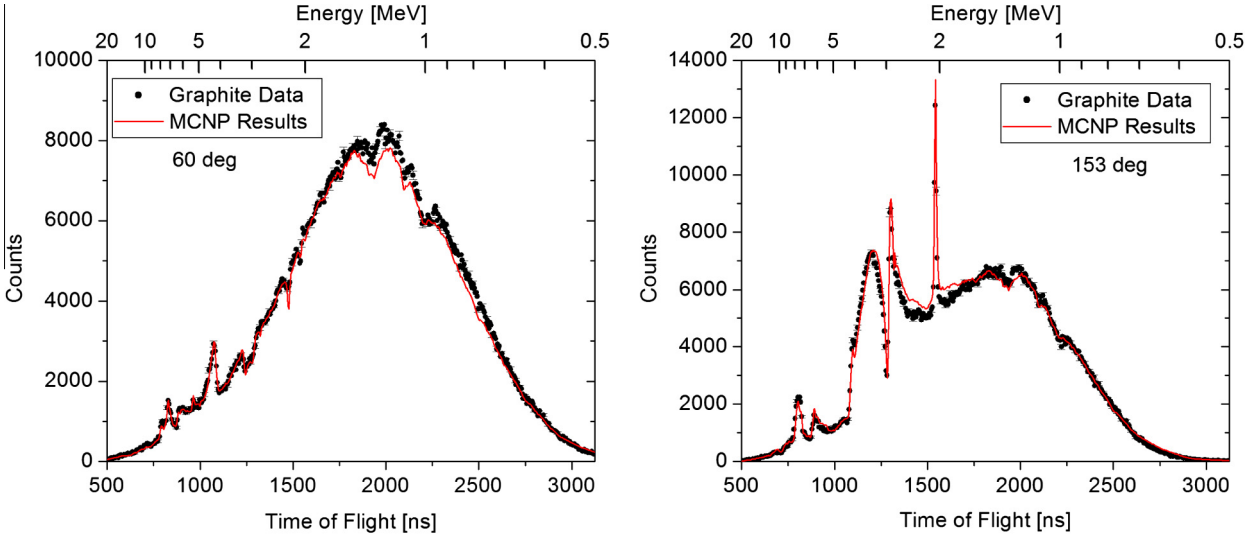

Fig. 6. Detectors 2 (left) and 3 (right) located at 60° and 153°, respectively, with respect to the incident neutron beam. The experimental data collected was part of the second set of angles.

whole ROI the FOM, as shown in Eq. (5), made it possible to determine which datasets compared most favorably with the ^{238}U experimental data.

Experimental data were collected by 8 detectors located at seven distinct angles over the course of two different experiments. As a consistency check two detectors were paired at each angle. Detectors 3 and 4, which were located at ≈154°, remained in the same positions for the two experiments, help to verify reproducibility between the two experiments.

6. Results and discussion

The angles for all detectors, shown in Table 3 and Figs. 6–16, have an accuracy of ±2°. The JENDL-4.0 evaluation agreed best with the experimental data based on the FOM for twelve measurements with detectors positioned at 27°, 29°, 60°, 77°, 112°, 113°, 130° (both detectors), 153° (both sets of angles), and 156° (both sets of angles). The largest distinction between JENDL-4.0 and the other ^{238}U evaluations was their performance for the detectors 3 and 4 located at extreme back angles of 153° and 156°, respectively. For both sets of angles the JENDL-4.0 outperformed the other evaluations as shown in Figs. 10 and 14. For detectors 1 and 7, located at 27° and 29°, respectively for the first set of angles, JENDL-4.0 was the only evaluation that adequately matched both sets of experimental data. The FOM values, available in Table 4, show the best-fitting evaluations and those that fall within 0.6 of its value, determined by sensitivity analysis as previously stated. Overall the ^{238}U FOM is larger than the graphite and thus still can be improved. In some cases the FOM of graphite is larger than the FOM of ^{238}U which indicates that the uncertainties of the experiment are sufficiently low to possibly also improve carbon scattering evaluations.

The ENDF/B-VII.1 evaluation agreed with eight measurements with detectors located at 27°, 45°, 77° (both detectors), 112°, 113°, and 130° (both detectors). At 112° and 113° the ENDF/B-VII.1 evaluation had the best agreement as seen in Fig. 9. For detectors 2 and 8, both located at 77° in for the first set of angles, ENDF/B-VII.1 was the only evaluation to match both sets of experimental data. Lastly, the JEFF-3.1 evaluation matched two measurements at 27° and 77°. And the ENDF/B-VI.8 library failed to agree with any experimental measurements. All MCNP fits to the ^{238}U experimental data are available in Figs. 7–10 and from Figs. 11–14 for the first and second experiment, respectively.

Table 4
FOM comparing the experimental data and the MCNP calculations. Each FOM was calculated over the entire ROI, from 0.5 to 20 MeV. For ^{238}U, all values within 0.6 of the lowest FOM represent the best-fitting libraries and are shown in bold text.

Angle	Detector	Experiment	ENDF/B-VII.1	ENDF/B-VI.8	JENDL-4.0	JEFF-3.1	Graphite
27	1	1	**3.08**	4.38	**2.71**	**2.51**	2.48
29	7	1	5.34	4.68	**3.66**	4.41	1.55
45	7	2	**6.05**	30.20	8.42	10.92	3.23
60	2	2	**3.78**	7.88	**3.34**	5.00	2.87
77	2	1	**1.78**	3.06	2.60	**1.92**	1.37
77	8	1	**1.26**	3.56	**1.12**	1.90	0.92
112	6	1	**1.55**	9.47	**1.96**	2.31	3.48
113	5	1	**1.22**	7.63	**1.41**	2.09	3.19
130	5	2	**5.61**	20.90	**5.55**	8.86	3.90
130	6	2	**6.08**	20.81	**5.96**	9.31	3.63
153	3	1	6.23	4.79	**2.51**	6.90	3.00
153	3	2	12.60	13.11	**4.66**	14.65	6.04
156	4	1	8.40	3.89	**3.13**	8.41	2.31
156	4	2	17.91	10.78	**6.20**	18.65	5.03
Average	–	–	5.77	10.37	**3.80**	6.99	3.07

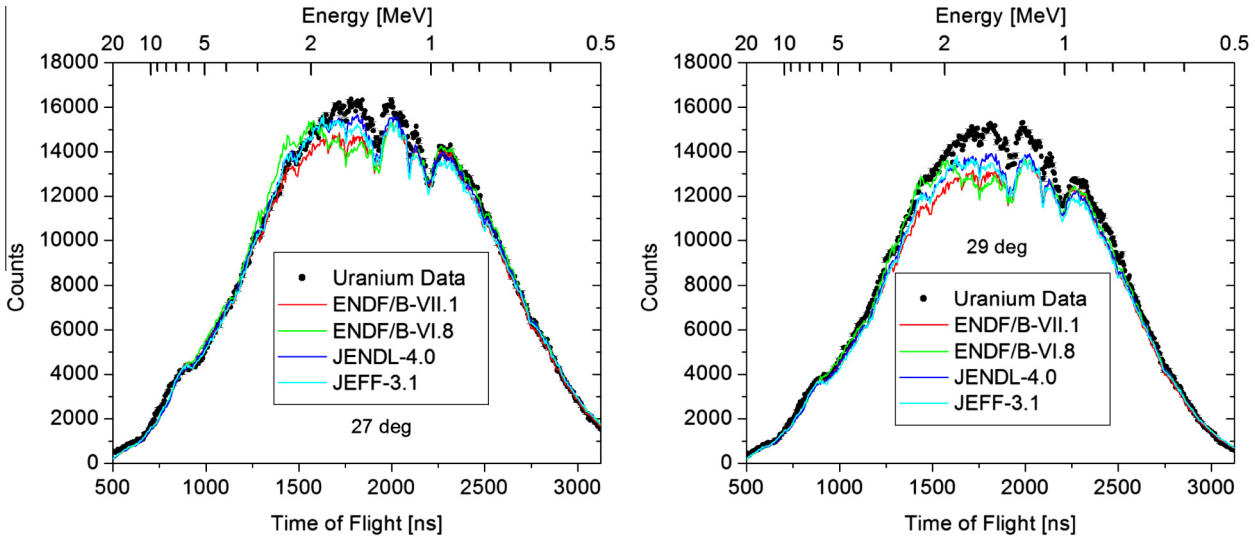

Fig. 7. Detectors 1 and 7 located at 27° and 29°, respectively, relative to the incident neutron beam. For both detectors the JENDL-4.0 evaluation best fits the experimental data.

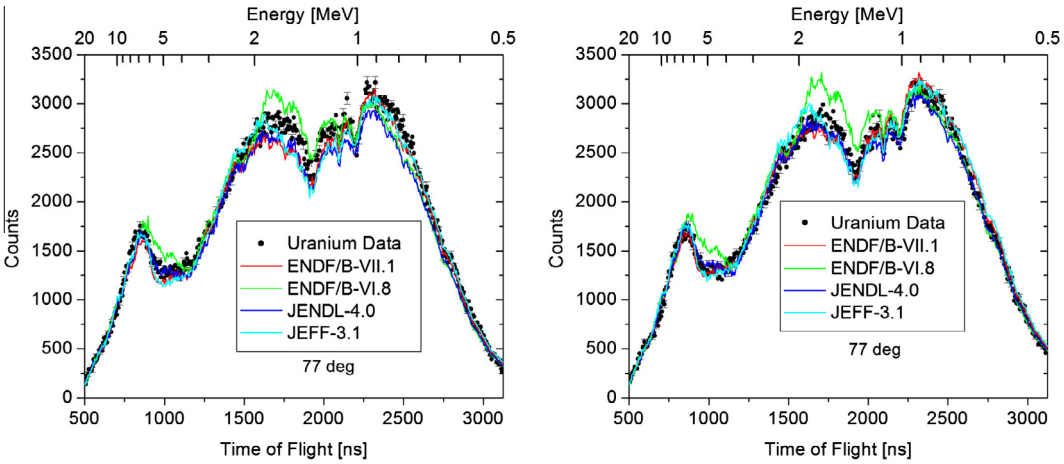

Fig. 8. Detectors 2 (left) and 8 (right), respectively, both located at 77° with respect to the incident neutron beam. For both detectors the ENDF/B-VII.1 evaluation best fits the experimental data.

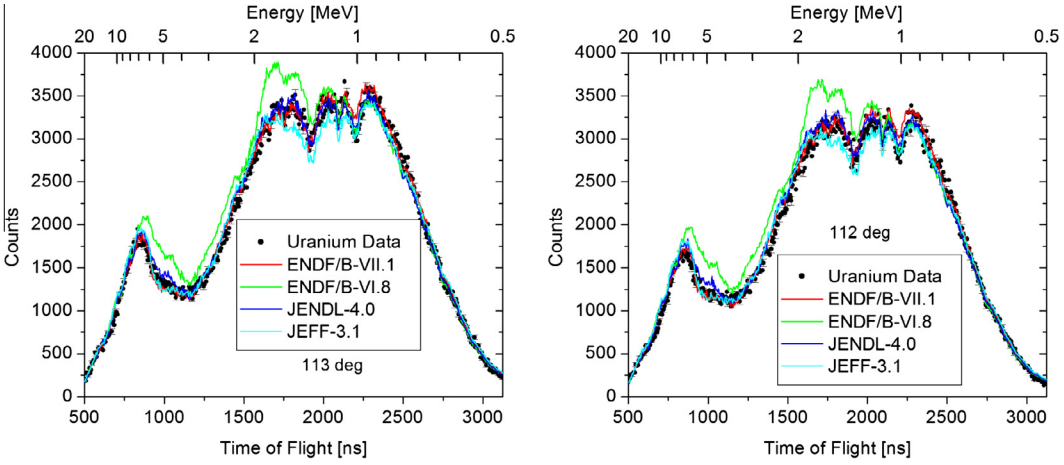

Fig. 9. Detectors 5 (left) and 6 (right) located at 113° and 112°, respectively, with respect to the incident neutron beam. For both detectors the ENDF/B-VII.1 and JENDL-4.0 evaluations fit the experimental data.

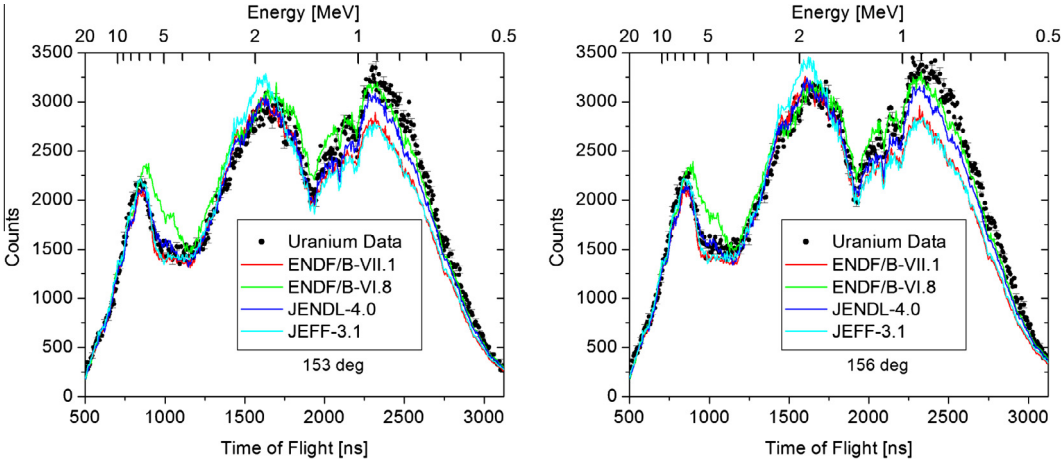

Fig. 10. Detectors 3 (left) and 4 (right) located at 153° and 156°, respectively, with respect to the incident neutron beam. For both detectors the best fitting evaluation was JENDL-4.0. ENDF/B-VII.1 and JEFF-3.1 underestimate the neutron response below ≈1 MeV while ENDF/B-VI.8 overestimates the response above ≈3 MeV. The experimental data collected was part of the first set of angles.

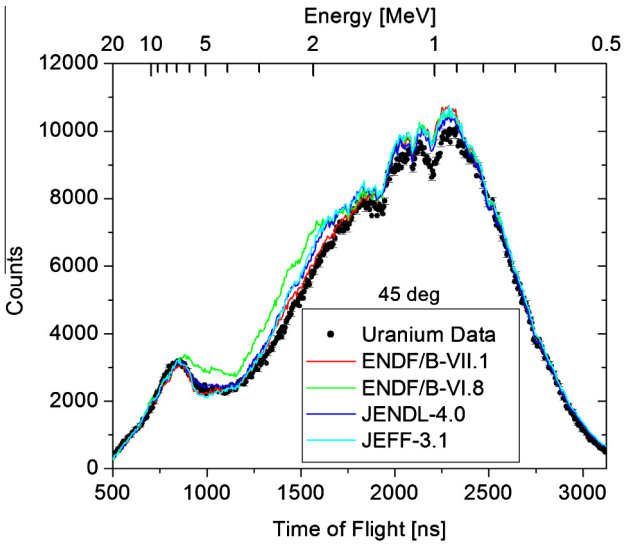

Fig. 11. Detector 7 located at 45° with respect to the incident neutron beam. The ENDF/B-VII.1 evaluation best fits the experimental data.

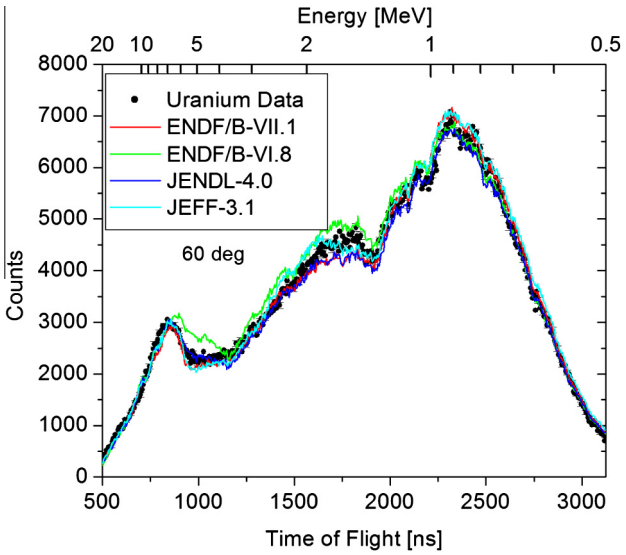

Fig. 12. Detector 2 located at 60° with respect to the incident neutron beam. The JENDL-4.0 evaluation best fits the experimental data.

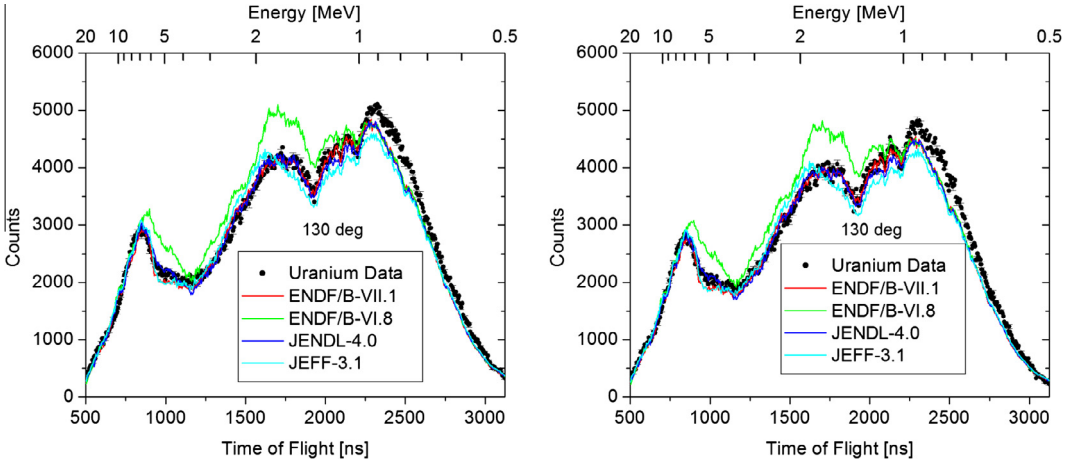

Fig. 13. Detectors 5 (left) and 6 (right) both located at 130° with respect to the incident neutron beam. For both detectors the ENDF/B-VII.1 and JENDL-4.0 evaluations fit the experimental data.

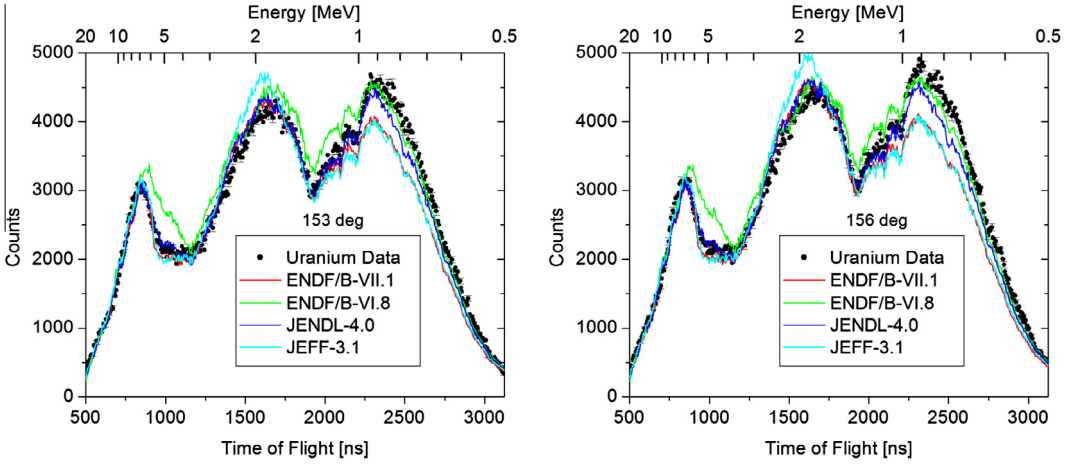

Fig. 14. Detectors 3 (left) and 4 (right) located at 153° and 156°, respectfully, with respect to the incident neutron beam. For both detectors the best-fitting evaluation was JENDL-4.0. The experimental data collected was part of the second set of angles. Similar to the previously presented results (Fig. 10) for these detectors, ENDF/B-VII.1 and JEFF-3.1 underestimate the neutron response below ≈1 MeV while ENDF/B-VI.8 overestimates the response above ≈3 MeV.

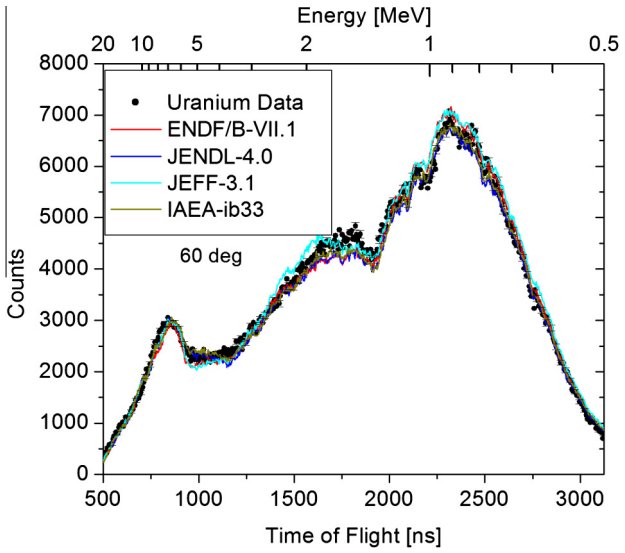

Fig. 15. Detector 2, located at 60 with respect to the incident neutron beam, during the second set of experimental data. The IAEA evaluation was used with MCNP featuring the same criteria as the other libraries. IAEA-ib33 evaluation had a slightly better fit than JENDL-4.0 and outperformed the other evaluations.

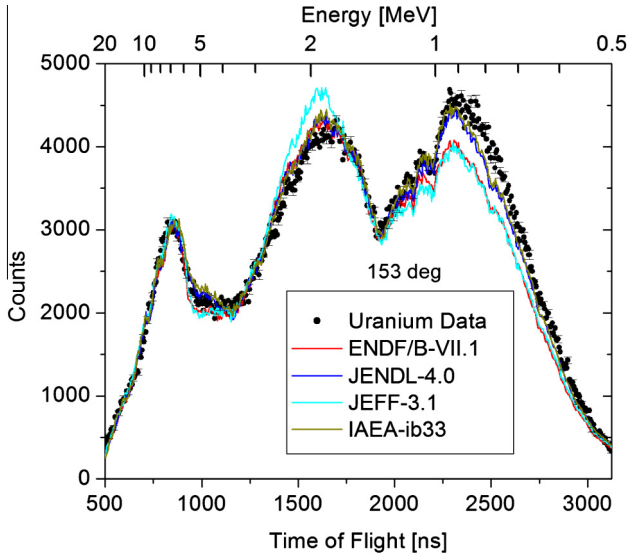

Fig. 16. Detector 3 with the second set of experimental data. The IAEA evaluation was used with MCNP featuring the same criteria as the other libraries. IAEA-ib33 evaluation was a slightly better fit than the JENDL-4.0 evaluation, which was significantly better than the other evaluations.

Table 5
The results of the IAEA dataset compared with the experimental data for two angles. In the cases shown, the IAEA dataset performed as well or better than the other ^{238}U evaluations based on the FOM used in this work.

Detector	Angle	Experiment	IAEA-ib33
Detector 2	60	2	2.86
Detector 3	153	2	4.37

A significant step for advancing the RPI scattering system as a benchmark to validate nuclear data was made through collaboration with Capote et al. (2014). Ongoing development of the IAEA ^{238}U nuclear data library included the process of analyzing its performance with respect to the quasi-differential data collected by the RPI neutron scattering system. This experimental data analysis allows an evaluator to adjust model parameters, including angular elastic and inelastic scattering, which have a prominent role in each integral benchmark tested with their ^{238}U evaluation. The FOM comparing ^{238}U data for detector 2, located at 60° during the 2nd set of angles, with the IAEA-ib33 evaluation had a better fit than JENDL-4.0 and shows an improvement over all other evaluated data libraries. For detector 3, located at 153°, the IAEA-ib33 evaluation had a slightly better fit compared with the JENDL-4.0 evaluation. The results of these calculations are shown in Table 5 and Figs. 15 and 16.

7. Conclusions

An improved model of the RPI neutron scattering system was developed that included a new neutron flux measurement and individual detector efficiencies based on in-beam measurements performed with a ^{235}U fission chamber and EJ-301 detectors. Data analysis featured gamma misclassification correction that improved conventional pulse shape analysis by removing contamination due to misclassified gamma events. This was essential due to the large gamma production from fission and inelastic scattering. Evaluations were compared with experimental data using a FOM that accounted for statistical and systematic uncertainties. It was concluded that the JENDL-4.0 evaluation performed closest to the measured ^{238}U data for a majority of the angles measured. Although JENDL-4.0 agreed best with the experimental data, overall the FOM for graphite is lower than ^{238}U which indicates that there is still room for improvement in the ^{238}U evaluations. In addition, an MCNP calculation using the IAEA-ib33 evaluation provided essential feedback in the ongoing development of the IAEA ^{238}U nuclear data library that is relevant to the international CIELO collaboration (Chadwick et al., 2013).

Acknowledgments

The authors would like to thank the RPI LINAC staff and operators: Peter Brand, Mathew Gray, Martin Strock, and Azeddine Kerdoun. The data presented in this publication would not be possible without their time and effort.

The JSI contribution to the IAEA-ib33 evaluation was partly supported by the 7-th European Framework Program through the ANDES project.

References

Barry, D.P. et al., 2013. Quasi-differential neutron scattering in zirconium from 0.5 MeV to 20 MeV. Nucl. Sci. Eng. 174 (2), 188–201.
Capote et al., 2014. Physics of Neutron Interactions with ^{238}U: new developments and challenges. Nucl. Data Sheets 118, 26–31.
Chadwick, M.B., Herman, M., Oblozinsky, P., et al., 2011. ENDF/B-VII.1 Nuclear data for science and technology: cross sections, covariances, fission product yields and decay data. Nucl. Data Sheets 112 (12), 2887–2996.
Chadwick, M.B., et al., 2013. CIELO, A future collaborative international evaluated library In: ND2013, International Conference on Nuclear Data for Science and Technology, New York, New York, United States of America, March 4–8.
Knoll, G.F., 2000. Radiation Detection and Measurement. Wiley & Sons, New York.
Koning, A., Forrest, R., Kellett, M., 2006. The JEFF-3.1 Nuclear Data Library. Nuclear Energy Agency, ISBN 92-64-02314-3.
Maslov, V.M. et al., 2003. Neutron Data Evaluation of ^{238}U. International Atomic Energy Agency Report INDC(BLR)-014, March, 2003.
MCNP, 2005. A General Monte Carlo Code for Neutron and Photon Transport, Version 5, LA-UR-05-8617.
Mosteller, R.D., MacFarlane, R.E., 2006. Comparison of results for the MCNP criticality validation suite using ENDF/B-VII and other nuclear data libraries. In: PHYSOR 2006, Vancouver, British Columbia, Canada, September 10–14, 2006, American Nuclear Society.
National Nuclear Data Center (NNDC) at Brookhaven National Laboratory (BNL), Website: <http://www.nndc.bnl.gov>, Retrieved 05-01-2013.
Overberg, M.E. et al., 1999. Photoneutron target development for the RPI linear accelerator. Nucl. Instrum. Methods Phys. Res. A 438 (2–3), 253–264.

Saglime, F.J., 2009. High Energy Nuclear Differential Scattering Measurements for Beryllium and Molybdenum (Ph.D. thesis). Rensselaer Polytechnic Institute.
Saglime, F.J. et al., 2010. A system for differential neutron scattering experiments in the energy range from 0.5 to 20 MeV. Nucl. Instrum. Methods Phys. Res. A 620 (2–3), 401–409.
Savitzky, A., Golay, M.J.E., 1964. Smoothing and differentiation of data by simplified least-squares procedures. Anal. Chem. 36 (8), 1627–1639.
Scintillator Full Response to Neutron Detection (SCINFUL), PSR-0267, Oak Ridge National Laboratory, 1998.
Shibata, K. et al., 2011. JENDL 4.0: a new library for nuclear science and engineering. J. Nucl. Sci. Technol. 48 (1), 1–30.
Smith, A.B., Holt, R., Whalen, J., 1978. Argonne National Laboratory Report, ANL/NDM-43.